Applied Acoustics 211 (2023) 109538

Contents lists available at ScienceDirect

Applied Acoustics

journal homepage: www.elsevier.com/locate/apacoust

Reconfigurable coding acoustic meta-lens based on helical metamaterials

Xiang Li, Jian Li, Xinjing Huang *

The State Key Laboratory of Precision Measurement Technology and Instruments, Tianjin University, Tianjin 300072, China

ARTICLE INFO

Article history:
Received 27 March 2023
Received in revised form 5 June 2023
Accepted 9 July 2023
Available online 18 July 2023

Keywords:
Acoustic coding *meta*-lens
Helical structure
Reconfigurable focusing
Acoustic metamaterial

ABSTRACT

Acoustic lenses play an important role in acoustic sensing and imaging. We propose a reconfigurable coding *meta*-lens (RCML)based on helical metamaterials in the air. The proposed RCML consists of many reassemblable helical *meta*-units and tunnel-units that have stable phase-shift difference π; these two kinds of antiphase units are called logical "1{\Prime} and "0". By specific array arrangement, the units "1" and "0" can form RCML with different discretization particle sizes. We suggest a set of design and reconfiguration methods for RCML, which can modify the focus via small-scale adjustment. Both simulations and experiments demonstrate that the RCML can realize acoustic convergence over a wide designed frequency band with a compact volume. For low-frequency acoustic waves, the thickness of the RCML is only 1/5.7 the wavelength. Moreover, RCML exhibit accurate focus point control and great amplification effect. Our study has great potential in versatile applications, including the design of acoustic sensors, energy collection devices and imaging systems.

1. Introduction

The high-intensity convergent acoustic fields via acoustic focusing have been playing an important role in medical treatment [1,2] and non-destructive testing [3]. By a specific array arrangement, conventional directional sources change the angle of acoustic radiation to form a convergent beam. However, conventional acoustic focusing devices have complex construction and huge size (larger than the working wavelength), which increases the manufacturing cost and limits the application scenarios. In addition, conventional focusing lenses are restricted by Rayleigh's criterion to achieve high resolution.

Due to superior control over wavefronts, acoustic metamaterial (AM) has attracted extensive attentions to solve the above problems. metamaterial-based acoustic *meta*-lenes break the diffraction limit and can realize acoustic lens devices with precise convergence control. The thickness is much smaller than the working wavelength, which makes it a more compact system and increases the compatibility of acoustic lens devices with other components. AM has been used to construct various transmission or reflection *meta*-lenses for sensing [4], isolation [5–7], energy harvesting [8–11], and acoustic imaging [12–15]. Chen *et al.* [16] used a hole-structured *meta*-lens to realize a sub-wavelength imaging system with high spatial resolution, high contrast and wide working bandwidth. Han *et al.* [17] proposed a groove-structured acoustic lens to achieve near-field convergence, and analyzed the effect of groove depth and asymmetry on the broadband. Instead of using gradient attributes, Chiang *et al.* [18] proposed a new design method of constructing a *meta*-lens using metagratings-arrays of discrete scatters with coarser features for energy harvesting of ultrasonic waves. Lu *et al.* [19] developed a Luneburg-lens based cylindrical metamaterials that have good acoustic impedance matching and sidelobe elimination capability.

The above-mentioned *meta*-lenses stem from highly integrated design concept; if the focal point needs to be adjusted, the lens could no longer be reused and has to be completely redesigned and reprocessed. Moreover, large-scale integrated *meta*-lenses cannot be manufactured by 3D-printing, and can only be manufactured by traditional methods such as machining metals, which limit the freedom of structural design.

On the other hand, the *meta*-lens can be formed by arranging many regular discrete units to approximate the required phase distribution. Ma *et al.* [20] adopted a *meta*-surface unit with a single-cavity structure to construct a gradient *meta*-lens to realize underwater acoustic convergence with excellent broadband energy enhancement performance. Kim *et al.* [21] realized a *meta*-lens by using a space folding structure array, and analyzed the influence of visco-thermal losses and elastic deformation on the power transmission coefficients in detail. Li *et al.* [22] realized

* Corresponding author.
E-mail address: huangxinjing@tju.edu.cn (X. Huang).

https://doi.org/10.1016/j.apacoust.2023.109538
0003-682X/

a 2D circular *meta*-lens with the subwavelength acoustic Helmholtz resonator array, which shows high acoustic transmission efficiency for super-diffraction focusing. Jin *et al.* [23] reports a kind of gradient resonant pillars for stable deep subwavelength focusing and imaging of elastic wave in the plate. Recently, we report a 3D *meta*-lens [24] composed of discretely distributed *meta*-helicoid element to achieve accurate focus and enhances pressure amplitude about three times. For the above *meta*-lenses, the size of each unit is small, so each unit is relatively easy to fabricate. However, if the focus needs to be changed, the phase distribution will have to be redistributed and almost every unit needs to be modified. Because substantial new discrete units need to be redesigned to replace most unusable existing units, the cost of building such a new *meta*-lens is still very high. Therefore, most of the discrete *meta*-lenses with gradual phases cannot arbitrarily adjust focus in a convenient and economic method.

Recently, binary coding and reconfigurable *meta*-lenses provide a novel insight to solve this problem [25–27]. With only two kinds of *meta*-units that have a stable phase-shift difference, many discrete binary *meta*-units can accomplish *meta*-lens via elaborated array configuration. Tang *et al.* [28] utilized rectangular cavities to form Helmholtz resonators to achieve binary phase manipulation and implemented a 2D robust converging coding *meta*-lens. Zhao *et al.* [29] proposed a 2D broadband coding *meta*-surface, in which the *meta*-units are designed by using the bottom-up topology optimization method and two kinds of units can keep stable phase difference. Chen *et al.* [30] employed space folding structure to construct a 2D binary coding *meta*-surface to convergent acoustic waves in the air, and it has good performance in a specific frequency band.

However, most of the current coding *meta*-lenses are applying in 2D rather than 3D space, namely, the lens is not or cannot become axisymmetric about the sound axis and is more like a cylindrical lens rather than a spherical one, so they are unable to realize free 3D movement of focus via small-scale reconfiguration. More importantly, the above discrete coding *meta*-lenses lack standardized deployment and assembly process, the advantage of reusing a large part of *meta*-units is destroyed. In addition, because binary *meta*-units adopt local resonance structures or structures with a low spatial folding efficiency, these units generally have near half wavelength thickness and narrow bandwidth. These weaknesses have seriously limited the application scenarios and functions of binary phase coding *meta*-lens in real field.

In this work, we propose reassemblable helical *meta*-unit and tunnel-unit that have stable phase-shift difference π to form a binary phase coding *meta*-lens, which have a compact volume and tunable discretization particle size. Then, we propose a complete set of coding *meta*-lens design methods of moving the focus point with small-scale reconfiguration. Particularly, we also provide a combined sequence coding and representation method of the proposed *meta*-lens, which is of great significance for standardized automatic reassembly and reconfiguration. Simulations and experiments are carried out to demonstrate that the proposed reconfigurable coding *meta*-lens (RCML) can converge low-frequency acoustic waves with a flat compact structure, and have accurate focus control ability and broad working frequency band.

2. Theory and method

2.1. Binary units design

The hollow structures with and without helical metamaterial part form helical *meta*-unit and tunnel-unit with phase-shift difference π, and corresponds to the binary logic units "1{\Prime} and "0" respectively. Fig. 1 (a) shows the structural diagram of the unit "1", which is composed of connection linkers A and B, shell, helicoid, and central shaft. Fig. 1 (b) shows the structural diagram of the unit "0", which is the tunnel part after removing the central structure of the unit "1". By adjusting the pitch *P*, the unit "1" regulates the propagating path, so that the phase-shift is tuned on the outlet. Linkers A and B are connection structures for closely adhering or interlocking with each other.

In this paper, we choose the Velcro fabric as the connection type, and the hooks-face and piles-face are pasted on two opposite sides of the shell. Fig. 1(c) and (d) respectively show the sample photos of the units "1{\Prime} and "0", which are made of photosensitive resin via 3D printing. Since the density of the cured photosensitive resin is much higher than air, the channels can be regarded as hard boundaries, and the acoustic-solid coupling effects are ignored.

Fig. 1(e) and (f) respectively show the dimension definitions of the units "1{\Prime} and "0", whose specific values are shown in Table 1. It is worth noting that since the phase-shift of wavefront is uneven after the acoustic wave passing through the helical channel, the tunnel needs to extended by *E* to unify the phase-plane at the outlet.

Based on the effective medium theory [31], the unit "1{\Prime} can be regarded as an identical-size homogeneous *meta*-fluid, and its refractive index is expressed as:

$$n_{eff} = \frac{\sqrt{(\pi D_e)^2 + P^2}}{P} \tag{1}$$

Wherein, D_e is the effective diameter of the helicoid, and the effective ratio D_e/D is approximately to 0.46 for a *meta*-unit with D = 15 mm. Via adjusting *P*, different effective refractive indices n_{eff} can be obtained. It should be pointed out that because of adopted single-blade structure, the unit "1{\Prime} with a smaller *P* will not cause internal adhesion during 3D-printing. Compared with other helical metamaterials [32–35], the pitch *P* of the proposed structure has a loose scope restriction with P_{min} as small as 6 mm. In addition, according to the effective medium theory, it should be ensured that the maximum value of *P* is not greater than 1/5 of the applied wavelength, so $P_{max} = \frac{c_0}{f \cdot 5}$, where c_0 and f are acoustic velocity and working frequency respectively. Based on the theory of coding metamaterial [36,37], the phase-shift difference at the outlet between the units "1" and "0" should be π, and it is obtained that:

$$\frac{2\pi f \cdot n_{eff}}{c_0} \cdot L - \frac{2\pi f}{c_0} \cdot L = \pi \tag{2}$$

Combined with (1) and (2), we can derive the equation of working frequency:

$$f = \frac{c_0}{\frac{\sqrt{(D_e\pi)^2+P^2}}{P} - 1\nu \cdot 2L} \tag{3}$$

According to (3), the curves of *f* as a function of *P* with different *D* are shown in Fig. 2 (a) while keeping the unit "1{\Prime} have a stable phase-shift of π relative to the unit "0". It can be seen that the unit "1" has wide working frequency while obtaining a fixed phase.

Finite element simulation software COMSOL is used to obtain the transmission phase field when the input acoustic wave passes through the units "1{\Prime} and "0", and the results are shown in Fig. 2(b). The diversity combinations of *D* and *P* can achieve similar acoustic pressure field at the same *f*, which demonstrate that units with different sizes can play the same role, allowing for a more flexible discrete granularity of the *meta*-lens. Each group of phase-frequency curves of the probe points in Fig. 2(b) is shown in Fig. 2(c). It can be seen that the phases of the unit "1" change

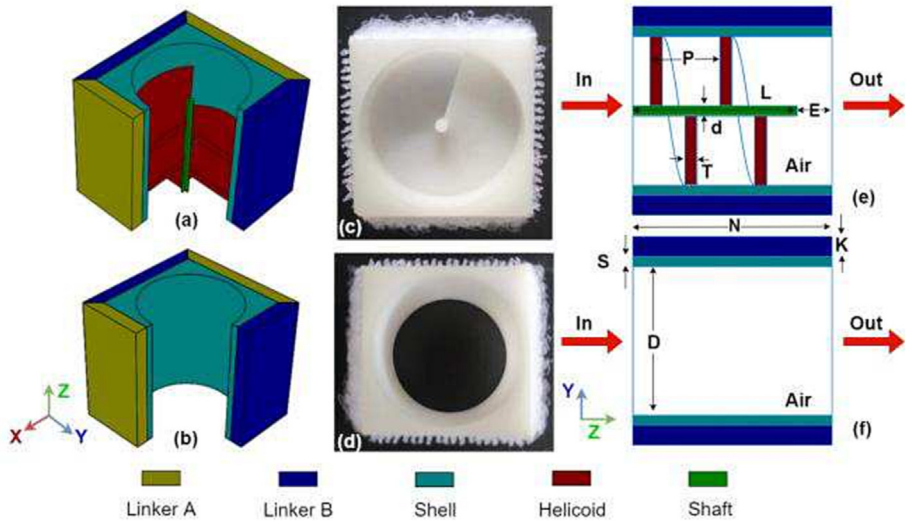

Fig. 1. Schematic diagrams of the unit "1{\Prime} and "0". (a)(b), (c)(d), and (e)(f) are structure details, sample photos and dimension definitions of the units "1" and "0", respectively.

Table 1
Geometric dimensions of the units "1{\Prime} and "0".

Name	Size	Description
T	1(mm)	Blade thickness
d	2(mm)	Shaft diameter
E	5(mm)	Extension length
S	1(mm)	Shell thickness
N	20(mm)	Thickness of unit
L	15(mm)	Length of helicoid
K	2.5(mm)	Linker thickness

approximately linearly with the frequency, and the difference with the unit "0" is stable around π. Notably, the *meta*-unit still maintains good phase manipulation capacity for import acoustic waves with low frequency (2500 Hz), whose wavelength is 6.8 times of the unit thickness N. The above results show that the units "1" and "0" have robust phase-shift difference over broadband in a compact volume, and exhibits good control over low-frequency wavefront.

2.2. Meta-lens coding and discretization

Fig. 3 shows the schematic of ideal phase-shift diagram for binary coding *meta*-lens, which can realize the converging lens by binary phase-shifts. The interval region is nominated as R_i $(i = 0, 1, \ldots)$ and blue and red represent phase-shifts of 0 and π, respectively. Each region is formed by extension of feature lines named S_i $(i = 1, 2, \ldots)$. Assuming that the transmitted acoustic waves are concentrated at the focal point (f_x, f_y, f_z), the difference between l_i

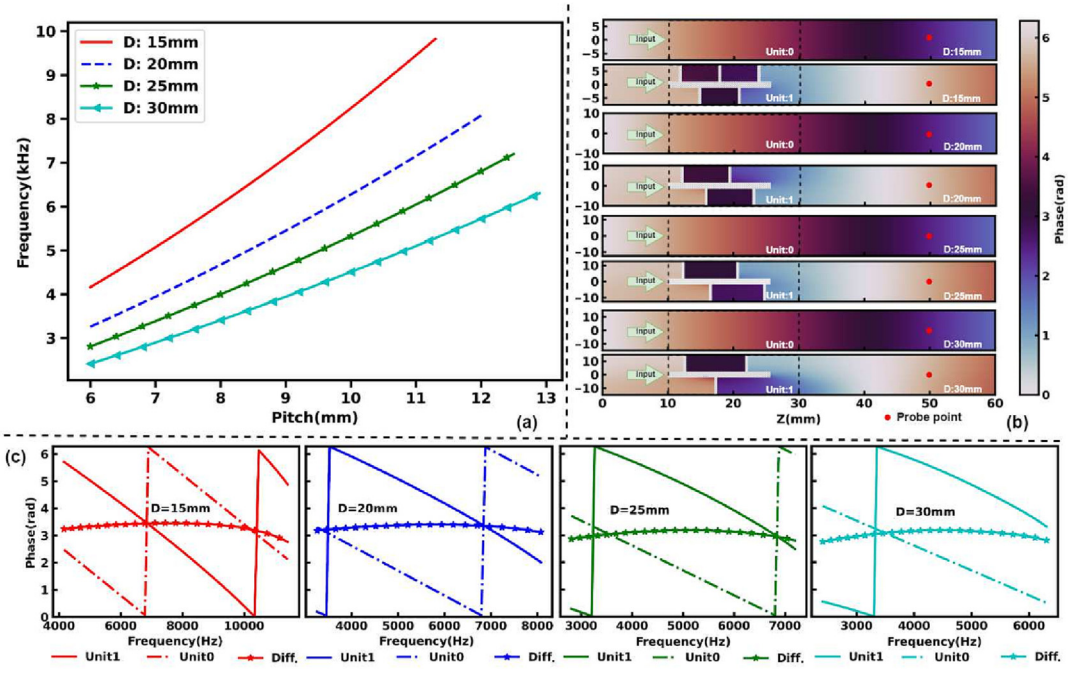

Fig. 2. Phase-shift between the units "1{\Prime} and "0". (a) f vs P of the unit "1" with different D. (b) Transmission phase fields of units "1" and "0" with different D. (c) Phase differences between the units "1" and "0" with different D.

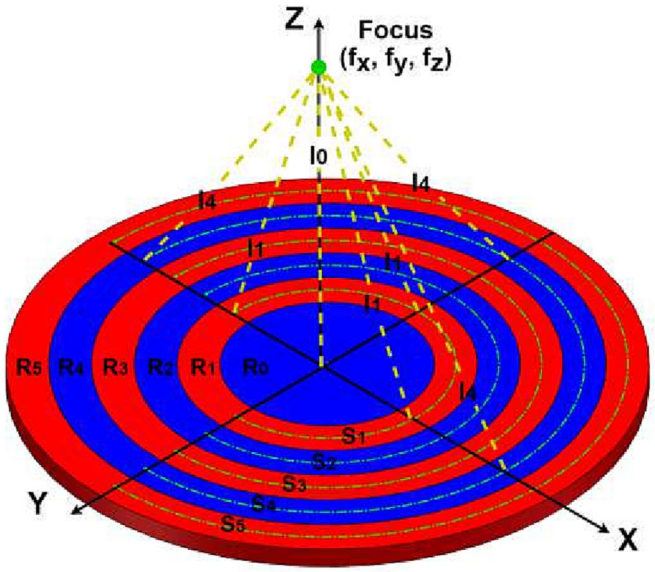

Fig. 3. Schematic of binary phase-shift coding *meta*-lens.

and l_0 is integer multiple of half the wavelength, which can be expressed as:

$$|l_i - l_0| = \frac{\lambda_0}{2} \cdot i (i = 1, 2, \cdots) \tag{4}$$

Wherein λ_0 is the acoustic wavelength for f; l_0 is the distance from the focus to the center point of the R_0 region, which can be expressed as:

$$l_0 = \sqrt{(f_x - x_0)^2 + (f_y - y_0)^2 + (f_z - z_0)^2} \tag{5}$$

Wherein $(x_0, y_0, z_0)$is the coordinate of the *meta*-lens center point in 3D space; l_i is the distance from the focus to the point within the feature line, which can be expressed as:

$$l_i = \sqrt{(f_x - s_{ix})^2 + (f_y - s_{iy})^2 + (f_z - s_{iz})^2} \tag{6}$$

Wherein (S_{ix}, S_{iy}, S_{iz}) is the coordinate of the point within the feature line. Combined with (4) (5) (6), we can get:

$$\left| \sqrt{(f_x - S_{ix})^2 + (f_y - S_{iy})^2 + (f_z - S_{iz})^2} - \sqrt{(f_x - x_0)^2 + (f_y - y_0)^2 + (f_z - z_0)^2} \right| = \frac{\lambda_0}{2} \cdot i \, (i = 1, 2, \cdots) \tag{7}$$

Only considering the scenario that the focus is on the Z axis, and the *meta*-lens center overlaps the origin, (7) is simplified as:

$$S_{ix}^2 + S_{iy}^2 = \left(\frac{\lambda_0}{2} \cdot i + f_z\right)^2 - f_z^2 \, (i = 1, 2, \cdots) \tag{8}$$

Observing (8), it can be found that the feature lines are circular, and its radius is related to the wavelength and focus. The in-phase annular area is developed from the feature line extension, and restricted by the two concentric circles:

$$\left(\frac{\lambda_0}{2} \cdot i + \frac{\lambda_0}{4} + f_z\right)^2 - f_z^2 \geq R_{ix}^2 + R_{iy}^2 \geq \left(max\left(\frac{\lambda_0}{2} \cdot i - \frac{\lambda_0}{4}, \, 0\right) + f_z\right)^2 - f_z^2 \, (i = 0, 1, 2, \cdots) \tag{9}$$

Wherein (R_{ix}, R_{iy}) mean the coordinate of any point in the i-th region, and even or odd of i corresponds to phase-shift annular of 0 or π respectively. As the positive integer i increases, one can calculate phase-shift expanded profile of the ideal coding *meta*-lens. According to (9), the ideal phase-shift profile of the coding *meta*-lens with a focal 80 mm at 6 kHz is calculated and shown in Fig. 4 (a), and the lens width and height are both 280 mm. The desired *meta*-lens is divided into phase-shift blocks by using square mesh for arranging the discrete units "1{\Prime} and "0". The particle size of the coding *meta*-lens is closely related to the mesh edge length (MEL). Fig. 4 (d) (e) (f) and (g) show the phase-shift profiles with MELs of 10 mm, 30 mm, 45 mm and 70 mm, respectively. It shows a smaller MEL generates a clearer in-phase annular, and the excessively large MEL leads to the disappearance of the region boundary.

Fig. 4(b) shows the phase-shift distributions along the diagonal lines of each *meta*-lenses with different MELs, and the smaller MEL brings the discrete lens more accurate phase match with the ideal lens. The matching ratios between the discrete *meta*-lenses and ideal *meta*-lenses in phase-shift lattice-points are calculated to illustrate the accuracy of the phase-shift distribution of the discrete *meta*-lens compared to the ideal *meta*-lens, as shown in Fig. 4(c). Therefore, a higher matching ratio means a closer approximation to the ideal phase-shift distribution. For example, the matching ratio of a *meta*-lens with 10 mm MEL can reach 93%, which is much greater than 50% with 70 mm MEL.

However, a decrease in MEL means a sharp increase in the number of regions. For example, to form a same-size *meta*-lens, a *meta*-lens with 10 mm MEL needs to be configured with 784 regions, while with 70 mm MEL the *meta*-lens only needs 16 regions. In summary, the discretization degree of coding *meta*-lenses, which is implemented with *meta*-units of different particle size, have the same tendency in terms of phase-shift matching ratio and configuration complexity.

2.3. Design process and reconfiguration scheme

Fig. 5 shows the complete process for RCML design and reconfiguration. Starting from requirement, we need to determine three groups of parameters to construct a definitely *meta*-lens: dimension parameters, including height and width, counts of rows and columns, and thickness; performance parameters, including frequency and focus range; auxiliary parameters, including connection type and manufacturing method.

The ideal phase-shift diagrams of the coding *meta*-lens are determined by the height, width, frequency range and focus range. The dimensions of the MEL are calculated by using the height and width and the count of rows and columns, and decide the square mesh to divide the ideal phase-shift profiles as a discrete phase-shift diagrams. Afterwards, a group of RCML phase-shift discrete diagrams is condensed into combination sequences by serialization method to facilitate information transfer and automatic assembly process. In addition, helicoid diameter D is determined by MEL, connection type and manufacturing method. Based on (3), the range of the P is deduced from the frequency range and D. In order to guarantee the phase sensitivity, P should not exceed the thickness of the *meta*-lens. Furthermore, according to geometric configurations and combination sequences, enough prefabricate units are manufactured to form unit library. The unit library contains several homo-frequency groups for different applications, in which the units have a fixed quantity and same specifications. Finally, all presupposed focus and frequency requirements can be fulfilled with uncomplicated reconfigurations.

Whenever a *meta*-lens to be reconfigured within the presuppose focus range, RCML can be reconfigured by retrieving the combination sequences and reassembling the units "1{\Prime} and "0".

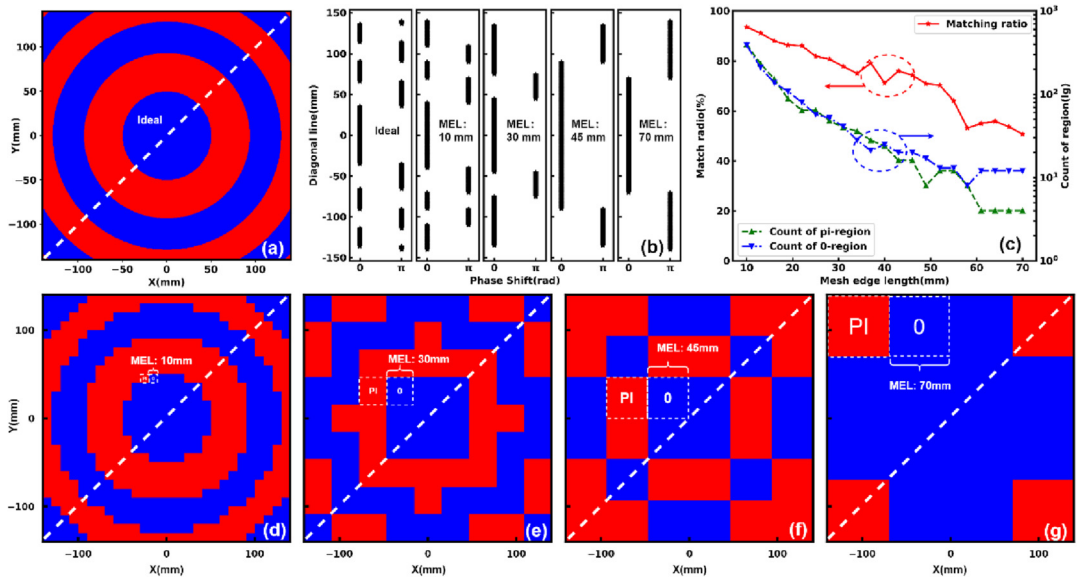

Fig. 4. Matching ratio and binary regions comparison of discrete coding *meta*-lenses with different particle sizes. (a) Ideal phase-shift profile of desired discrete *meta*-lens. (b) Phase-shift distributions along the diagonal lines of discrete *meta*-lenses with different MEL. (c) Matching ratio comparisons and binary regional quantity statistics. (d) (e) (f) (g) are the discretized phase-shift profile with MELs of 10 mm, 30 mm, 45 mm and 70 mm, respectively.

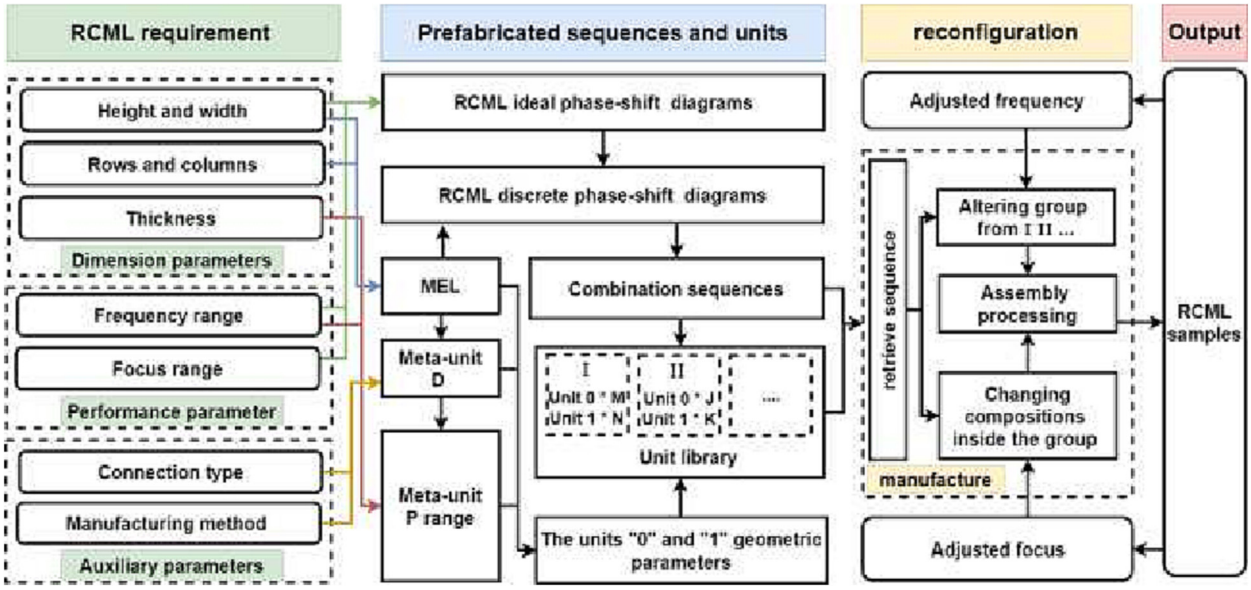

Fig. 5. RCML design and reconfiguration flow chart.

If the working frequency of RCML changes, it is necessary to alter library group before performing the above steps. Certainly, the assembly processing can be done with manual work or robot operation. It can be found that due to the characteristics of the coding *meta*-lens and the optimization process proposed in this paper, the reconfiguration of the *meta*-lens becomes convenient.

2.4. Serialize discrete phase diagrams

Different from the previous methods [6,38] that used diagrams and annotations to describe the *meta*-lens, this paper proposes a special representation method named combination sequence to indicate the *meta*-unit layout within *meta*-lens, which can simplify data hierarchy, particularly for giant *meta*-lens, and facilitates automated assembly, as is shown in Fig. 6(c). This representation is composed of the count expression "$R \times C$", the attribute expression "*G T L*" and column arrangement expression. Where, "*R*" and "*C*" respectively refer to the number of rows and columns. "*G*", "*T*", and "*L*" respectively refer to the number of the units for each group in each column, the date base and the focal length. "*T*" can be "B", "O", "D" and "H" that mean binary, octal, decimal and hexadecimal, respectively.

The specific layout of the *meta*-units is determined by the column arrangement expression, in which bits are one-to-one match *meta*-unit positions. The most significant bit (MSB) is on bottom, and the least significant bit (LSB) is on top. Fig. 6(a) and (b) show the layout of *meta*-lens for D = 25 mm and 15 mm, respectively. CLN0 and CLNn means the 0th and n^{th} columns of the *meta*-lens, respectively. Using the second column of Fig. 6(b) as an example, it can be expressed as "606{\Prime} with hexadecimal.

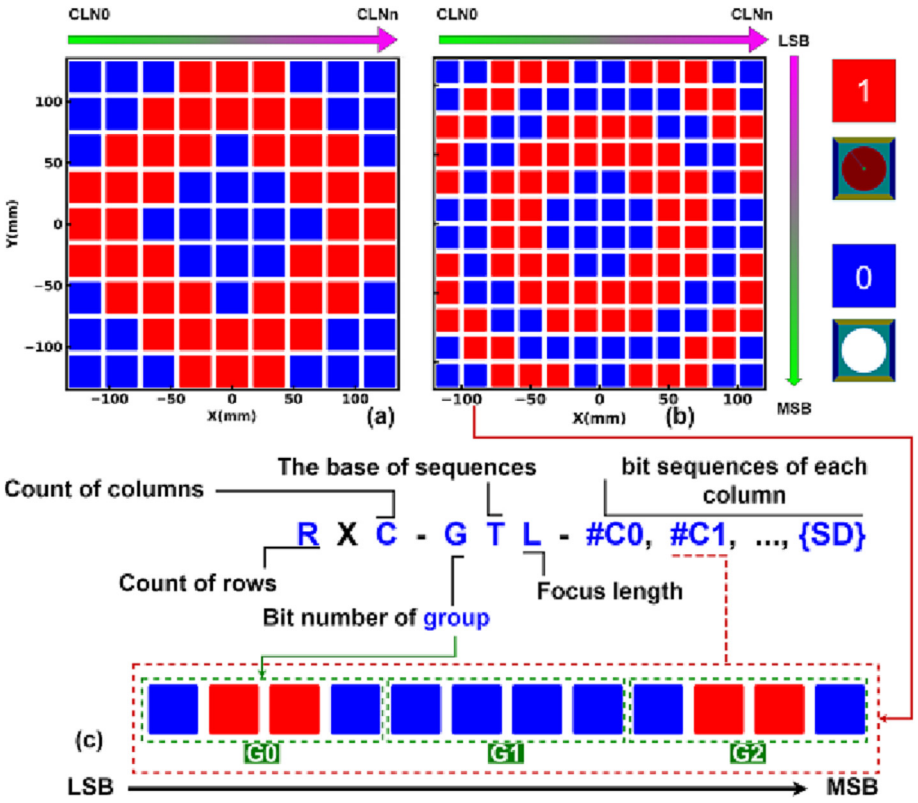

Fig. 6. Discretized layout and condensed representation method of *meta*-lens. (a) (b) are layout diagrams of *meta*-lens with 9 × 9 and 12 × 12 *meta*-units, respectively. (c) Serialization example for the second column of (b).

Furthermore, the combination sequences of Fig. 6(a) and (b) can be expressed as "070, 471, 653, 707, 306, SD", "C93, 606, 3FC, 9F9, D9B, C03, SD". "SD" means symmetrical distribution, which can reduce the sequence length. Therefore, the method can describe the RCML discrete phase-shift diagram as a definite combination sequence, which can simplify and standardize the annotations of the *meta*-lens and facilitates assembly.

3. Numerical simulation

We have designed six *meta*-lenses numbered as I, II, III, IV, V and VI, all of which have a dimension of 280 mm * 280 mm * 20 mm, and their parameters and combination sequences are listed in Table 2. Simulation as shown in Fig. 7(k) was carried out to test the acoustic focusing performances of those 6 *meta*-lenses. The *meta*-lens is surrounded by an air domain. For a clearer view, Fig. 7(k) shows only part of the air domain. Acoustic plane wave of 1 Pa is incident from the left surface of the air domain and converges on the right side of the *meta*-lens. Other surfaces of the air domain are set as radiation boundary conditions to prevent the influence of reflected waves. Acoustic-solid coupling and viscothermal effects are not considered in the simulation. Fig. 7(a)(e), (b)(f), (c)(g) and (d)(h) are the acoustic pressure field for I, II, III and IV in X-Y and X-Z planes that pass through the focus. It can be seen that all the six *meta*-lenses can achieve acoustic convergence in 3D space.

In order to quantitatively evaluate the acoustic convergence performance of the *meta*-lens, the acoustic pressure on the Z axis passing through the focus for each *meta*-lens is shown in Fig. 7 (i). The actual focal positions of *meta*-lenses I, II, and III are 38, 36, and 28 mm and the pressures at the focal points are 4.6, 2.9, and 5 times of the input acoustic pressure, which demonstrated the convergence and amplification capabilities of *meta*-lenses with different particle sizes. It is worth noting that *meta*-lens IV is one from reconfigured *meta*-lens III without changing the geometric parameters of the units "1{\Prime} and "0". *meta*-lens IV converges acoustic waves to the focus at 78 mm with amplified pressure of 3.2 times. Fig. 7(j) shows the acoustic pressure on the line parallel to Y axis and passing through the focus point. Because the *meta*-lenses are symmetrical, the acoustic pressure curves are also highly symmetrical.

There are noticeable sidelobes in Fig. 7(j), which are produced by abrupt changes of the modulated phase , due to the discontinuous phase-shift of wavefront [39]. There are several measures to

Table 2
Encoding Parameters of Six Meta-lenses.

Name	MEL (mm)	Frequency (Hz)	Focus (mm)	Meta-lens combination sequence
I	20	6000	50	14 × 14 – 4H 50 – 1F32, 8370, C0C0, 6E91, 3F33, B373, 9162, SD
II	30	4500	50	9 × 9 – 3O 50 – 306, 124, 471, 401, 603, SD
III	35	6000	50	8 × 8 – 4H 50 – DB, 24, DB, 5A, SD
IV	35	6000	80	8 × 8 – 4H 80 – 66, 99, DB, 66, SD
V	30	3000	50	9 × 9 – 3O 50 – 070, 471, 653, 707, 306, SD
VI	30	6000	50	9 × 9 – 3O 50 – 471, 202, 174, 555, 505, SD

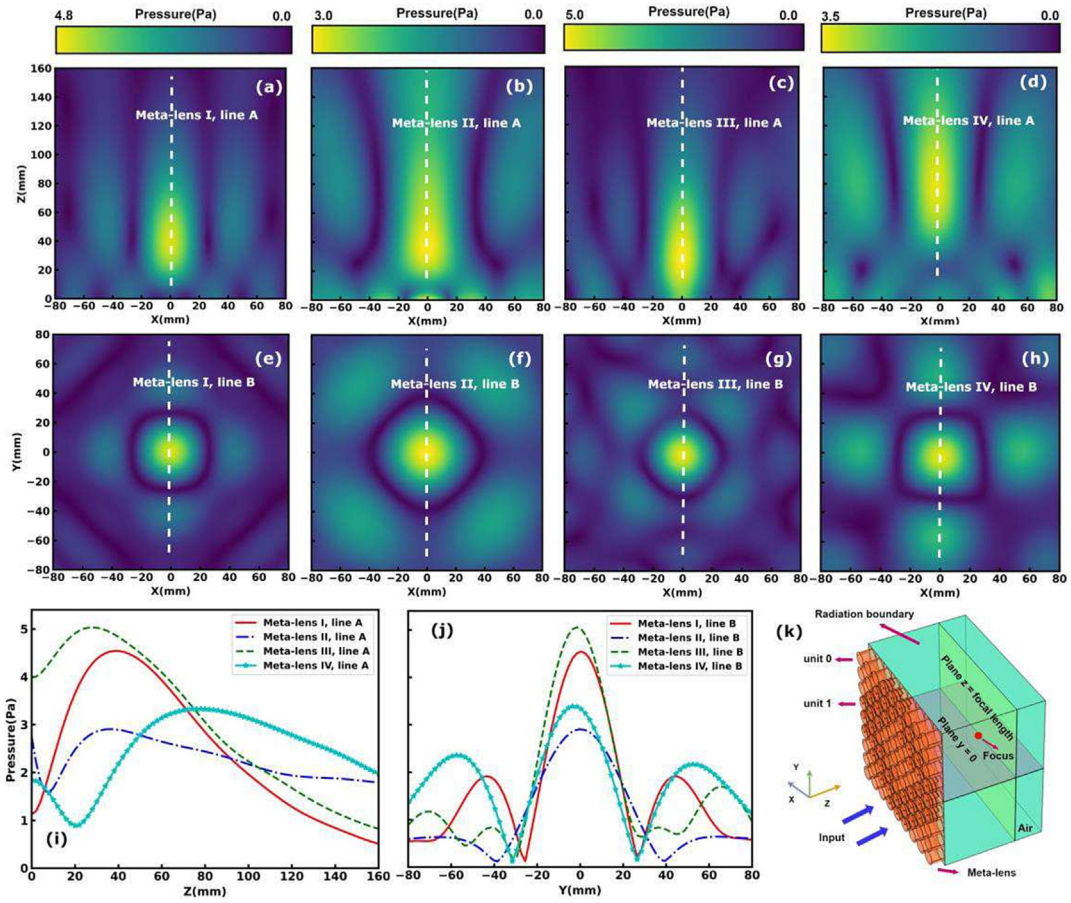

Fig. 7. Simulation results of RCMLs. (a)(b)(c)(d) Acoustic pressure fields on the y = 0 plane passing through the focus. (e)(f)(g)(h) Acoustic pressure fields on the plane z = focal length. (i)(j) Acoustic pressure on lines of (a)-(h). (k) Meta-lens simulation diagram.

suppress the sidelobes. We can learn from the suppression method of array antenna [40] to use, the RCML can apply a weighting function to the input acoustic amplitudes by transforming some "0{\Prime} units into solid units, and then achieve the sidelobes suppression. In addition, it is also feasible to achieve the suppression of sidelobes by multiplexed beam summation method [41]. Therefore, it is possible to suppress the sidelobes of the RCML by transforming part of the functions of the "1{\Prime} and "0{\Prime} units, but it may reduce the transmission ratio and extend the focal spot area. According to the above results, all the RCMLs with different MELs can work well with different focuses and working frequencies.

If the focus point needs to be changed, *meta*-lens only needs to reconfigure the units "1{\Prime} and "0{\Prime} distribution. Fig. 8 shows how many of the compositions in the *meta*-lens III change as the focal point is moved from 20 mm to 100 mm. It can be seen that the maximum number of changed components caused by the focus movement is 16, and the average is 4, only about 6% of the total. For all the *meta*-lenses, only a small part of the 44 units "1{\Prime} and the 40 units "0" need to be reconfigured. It should be emphasized that unlike former implementation schemes of *meta*-lenses using highly integrated or polytyped units, the proposed RCML has good reconfigurability and is low cost.

In order to illustrate the broadband of the *meta*-lens, the frequency responses of the *meta*-lenses V II and VI are respectively investigated via sweeping-frequency simulations from 2000 to 5700 Hz, 3200 Hz to 8000 Hz and 3900 Hz to 9000 Hz, and the results are shown in Fig. 9. Furthermore, we calculated the quality factors of the *meta*-lenses, which can be defined as $Q = f_0/\Delta f$, where f_0 and Δf represent the center frequency and bandwidth, as sketch shown in the inset. The Q of *meta*-lenses V, II and VI are 1.8, 1.7 and 2.1, respectively, which are very low. Therefore, the RCMLs proposed by this paper have a wide bandwidth.

To further demonstrate the acoustic fields of lenses V, II and VI at non-center working frequencies within the broadband, we demonstrate the acoustic pressure fields of lenses V, II and VI at 4300 Hz, 5500 Hz and 7000 Hz, respectively. Convergence fields in X-Z plane are shown in Fig. 10 (a) (b) and (c), and the convergence fields in the X-Y plane are shown in Fig. 10 (d) (e) and (f). It can be seen that the *meta*-lenses still have high focal pressures at the non-center working frequencies, which are consistent with Fig. 9 results. Therefore, the *meta*-lenses V, II and VI have great convergence performances within a wide band.

4. Experimental verification

An experiment system was built for acoustic field measurement to verify the acoustic focusing performance of *meta*-lens. Fig. 11 (a) shows the photos of fabricated *meta*-lenses V, II, VI, and Fig. 11 (b) shows the adopted 3D scanning measurement system. The single-frequency signal is generated by the function generator and then boosted by a power amplifier before transmitted to the loudspeaker. The loudspeaker is located several wavelengths away from the *meta*-lens to create a plane-like wave input. The acoustic signal behind the *meta*-lens is collected by the microphone, and the data acquisition board records signal. Particularly, the microphone is installed on the motorized slide table for three degrees

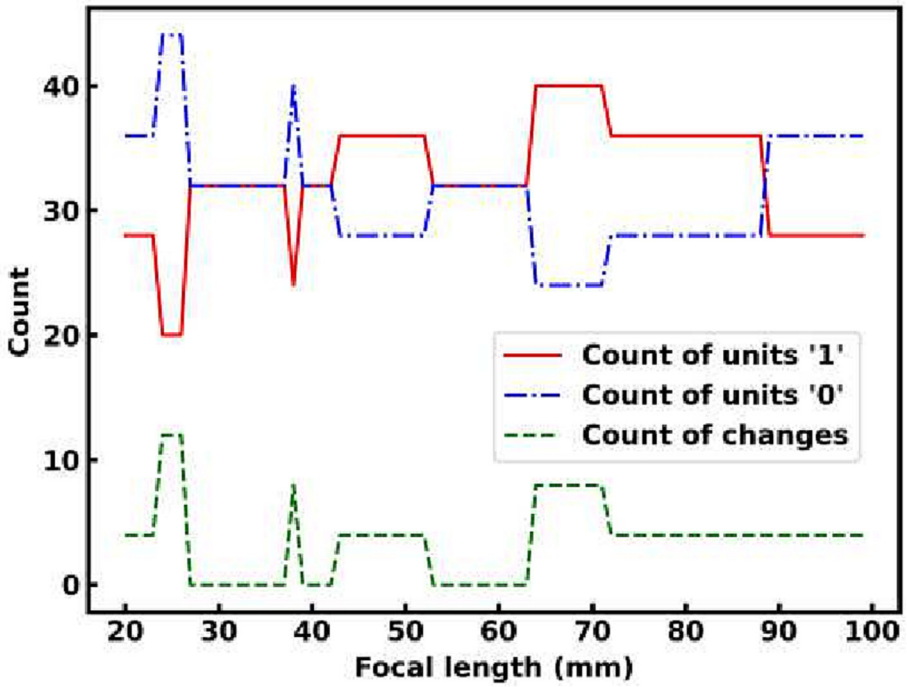

Fig. 8. Compositions of RCML and reconfigurations statistics.

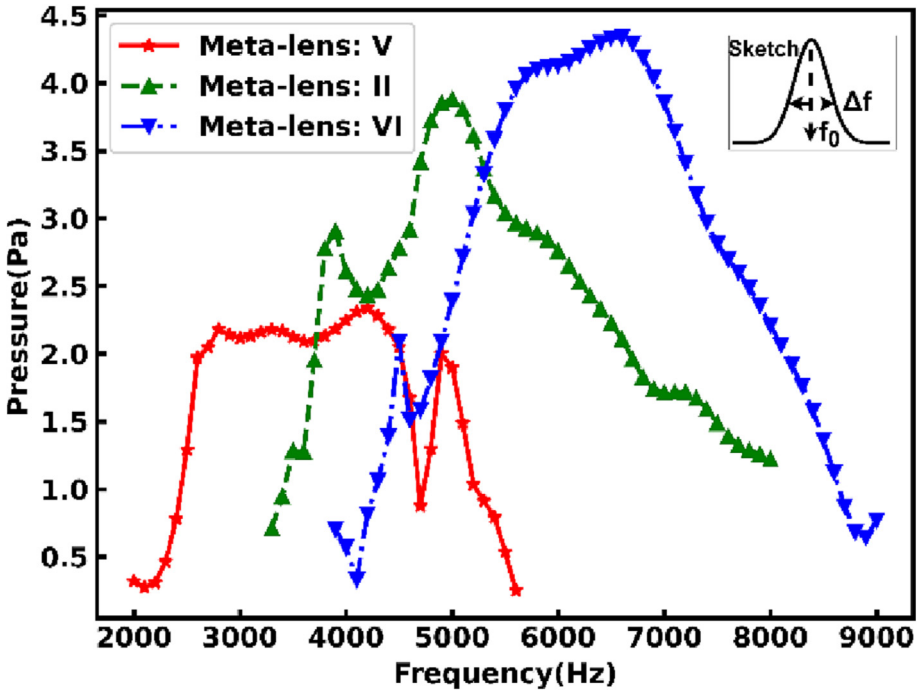

Fig. 9. Frequency responses of focal acoustic pressure for the V, II and VI *meta*-lenses.

of freedom moving, and scans X-Y and X-Z planes in zigzag path to measure acoustic field.

The 3 kHz sound is played for the *meta*-lens V, and the simulation and experimental results (inset) of acoustic pressure fields in X-Y and X-Z planes passing through the focus are shown in Fig. 12 (a) and (b), respectively. Simulation and experiment results are highly consistent, and the proposed RCML has a significant concentration effect for low-frequency acoustic waves whose wavelength is 5.7 times the *meta*-lens thickness. The acoustic pressure on lines in X-Y and X-Z planes are shown in Fig. 11(c).

Similarly, Fig. 12 (d) (e) (f) and (g) (h) (i) show the simulation and experiment results of the *meta*-lenses II and VI at 4.5 and 6 kHz, respectively. For different frequencies, the RCML can focus acoustic waves effectively, and the simulation results are consistent with the experiment results. The errors between the simulation and experiment are attributed to the manufacturing process of *meta*-units, assembly of RCML and visco-thermal loss, but these do not affect the main points and conclusions expressed in this paper. We used 3D printing technology to realize "0{\Prime} and "1{\Prime} units with a manufacturing accuracy error of 0.2 mm.

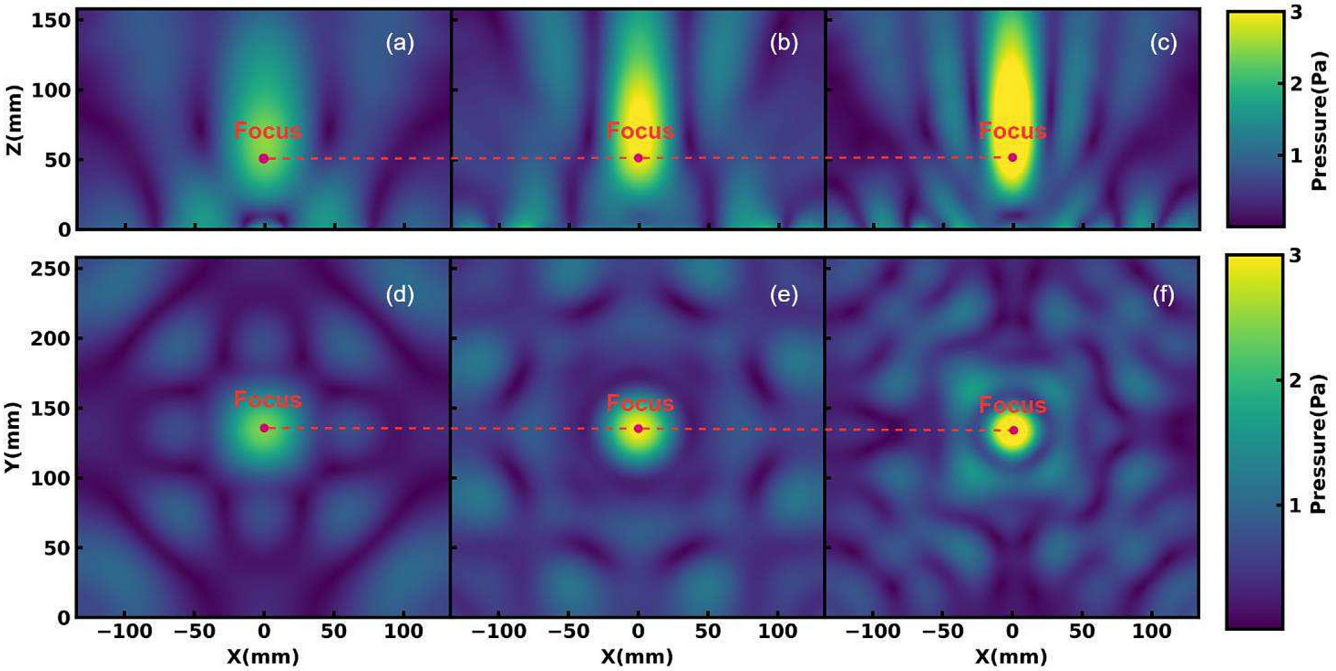

Fig. 10. Convergent fields of *meta*-lenses V, II and VI. (a) (b) and (c) are the convergence fields in the X-Z plane after the acoustic waves passing through *meta*-lenses V, II and VI at 4300 Hz, 5500 Hz and 7000 Hz, respectively. (d) (e) and (f) are the convergence fields in the X-Y plane after the acoustic waves passing through *meta*-lenses V, II and VI at 4300 Hz, 5500 Hz and 7000 Hz, respectively.

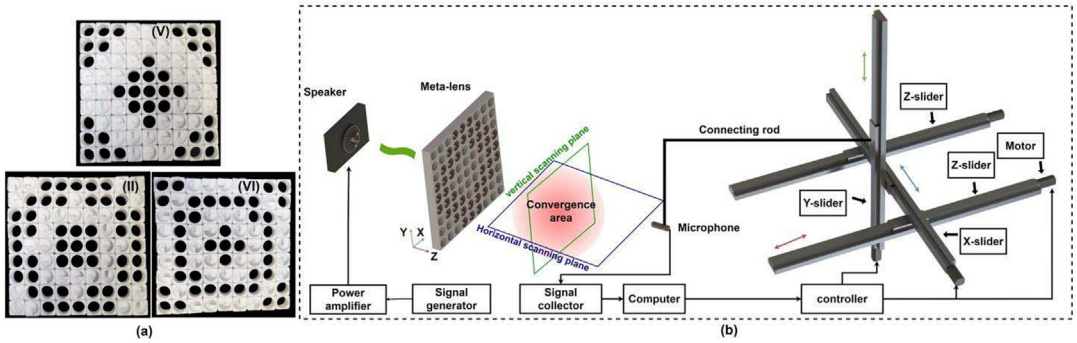

Fig. 11. Experimental method. (a) Photos of *meta*-lens V, II, VI. (b)Experimental setup.

Velcro is used as connection linkers by simply attaching to the "0{\Prime} and "1{\Prime} units. However, because of its elasticity of connections, the RCMLs have assembly errors and are slightly deformed due to gravity. If rigid magnetic shells are used as the connection linkers of the *meta*-units and a rigid fixed frame is made for the entire *meta*-lens, the deformations can be reduced, but to a certain extent increases the cost. Based on the Rayleigh criterion, the quality of spatial resolution is associated with the full width at half maximum (FWHM). The resolution of traditional lenses is quite low, and its FWHM is larger than the wavelength. In marked contrast, the FWHM of the advanced RCML are 0.52, 0.58 and 0.66 times of wavelength at frequencies 3, 4.5 and 6 kHz, respectively. Therefore, our proposed RCML can accurately and efficiently manipulate acoustic convergence at the sub-wavelength scale over a wide frequency range.

5. Conclusion

In this paper, a high-performance reconfigurable 3D binary coding *meta*-lens is realized by using helical *meta*-units and tunnel-units. With stable phase difference π, the binary units correspond to logic "1{\Prime} and "0{\Prime}. Different from the previous study, the unit "1{\Prime} and "0{\Prime} have a wide designed frequency band in compact size. Based on the characteristics of the units, we can construct coding *meta*-lenses named RCML with different particle sizes. We also propose a set of design and representation scheme, so that the RCML can be facilitated and assembled with automated and standardized method. Simulation and experiment results demonstrate that the RCML can effectively amplify acoustic wave with accurate focus control over a broadband. At the focus, the pressure can be magnified by $3 \sim 5$ times. Remarkably, we can move the focal of the RCML with very small-scale reconfiguration.

Our proposed compact RCMLs have wide working bandwidth and acoustic pressure amplification capabilities, and can be easily reconfigured to meet the needs of frequency and focus changes. we envision that the front lens designed by RCML can realize small size acoustic sensors and energy harvesting devices, with ability of effectively improving the sensitivity and signal-to-noise ratio of the sensors; good spatial resolution and wide bandwidth of the proposed *meta*-lenses can improve the accuracy of acoustic

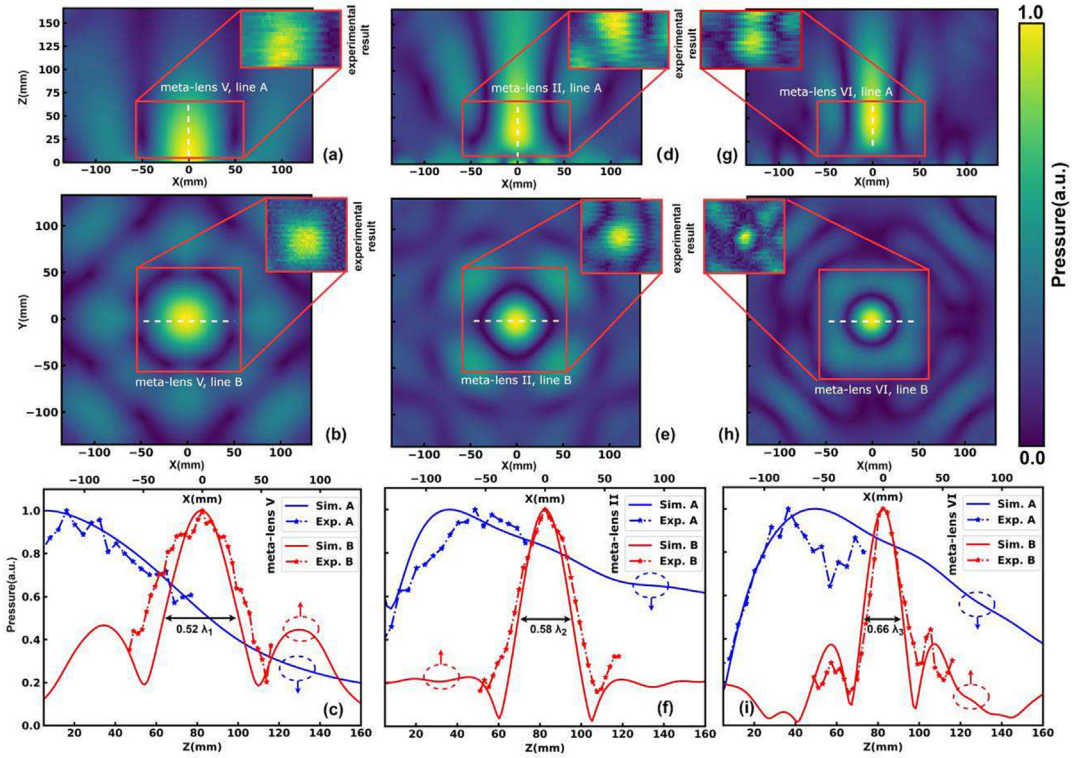

Fig. 12. Simulation and experimental results of RCMLs. (a) (b), (d) (e) and (g) (h) are the acoustic pressure fields on the X-Y and X-Z planes at 3, 4.5 and 6 kHz, respectively. (c), (f) and (i) are the acoustic pressure on lines in the X-Y and X-Z plane, respectively.

imaging. Further, these devices can meet the needs of the actual scenes for focal length and application frequency adjustments after simple reconfigurations. Therefore, our study has great potential in versatile applications, including the design of acoustic sensors, energy collection devices and imaging systems.

CRediT authorship contribution statement

Xiang Li: Conceptualization, Methodology, Investigation, Writing – original draft. **Jian Li:** Supervision, Validation. **Xinjing Huang:** Conceptualization, Investigation, Methodology, Funding acquisition, Resources, Supervision, Writing – review & editing.

Data availability

Data will be made available on request.

Declaration of Competing Interest

The authors declare that they have no known competing financial interests or personal relationships that could have appeared to influence the work reported in this paper.

Acknowledgements

This work was supported in part by Natural Science Foundation of Tianjin under Grant 21JCQNJC00690, Research Project of Tianjin Education Commission under Grant 2018KJ230 and State Key Laboratory of Precision Measuring Technology and Instruments under Grant pilab2104

References

[1] Lei W, Ren K, Chen T, Chen X, Li B, Chang H, et al. Polydopamine nanocoating for effective photothermal killing of bacteria and fungus upon near-infrared irradiation. Adv Mater Interfaces 2016;3(22):1600767.
[2] Huang H-Y, Liu H-L, Hsu P-H, Chiang C-S, Tsai C-H, Chi H-S, et al. A multitheragnostic nanobubble system to induce blood–brain barrier disruption with magnetically guided focused ultrasound. Adv Mater 2015;27(4):655–61.
[3] Brizuela J, Camacho J, Cosarinsky G, Iriarte JM, Cruza JF. Improving elevation resolution in phased-array inspections for NDT. NDT&E Int 2019;101:1–16.
[4] Chen T, Li W, Yu D. A tunable gradient acoustic metamaterial for acoustic sensing. Extreme Mech Lett 2021;49:101481.
[5] Wang M, Yi K, Zhu R. Tunable underwater low-frequency sound absorption via locally resonant piezoelectric metamaterials. J Sound Vib 2023;548:117514.
[6] Yan G, Yao S, Li Y. Propagation of elastic waves in metamaterial plates with various lattices for low-frequency vibration attenuation. J Sound Vib 2022;536:117140.
[7] Baena JC, Wang C, Fu Y, Kabir II, Yuen ACY, Peng Z, et al. A new fabrication method of designed metamaterial based on a 3D-printed structure for underwater sound absorption applications. Appl Acoust 2023;203:109221.
[8] Ahmed A, Sabra K, Erturk A. Sound energy harvesting by leveraging a 3D-printed phononic crystal lens. Appl Acoust 2021;118(10):103504.
[9] Ren Z, Dong H-W, He X, Chen M, Fang D. Underwater gradient metalens for broadband subwavelength focusing. Int J Mech Sci 2022;229:107521.
[10] Lei Y, Wu JH, Huang Z, Wang L, Huang Y. Broadband directional resonant tunneling emission enhancement via acoustic anisotropic metamaterials. Appl Acoust 2022;200:109050.
[11] Sun W, Zhong K, Liu Y, Xiao H, Zhao D, Yan Z, et al. Enhanced metamaterial vibration for high-performance acoustic piezoelectric energy harvesting. Compos Commun 2022;35:101342.
[12] Hu C, Weng J, Ding Y. Experimental demonstration of a three-dimensional acoustic hyperlens for super-resolution imaging. Appl Phys Lett 2021; 118 (20): 203504.
[13] Tian Y, Ge H, Zhang X-J, Xu X-Y, Lu M-H, Jing Y, et al. Far-field subwavelength Acoustic computational imaging with a single detector. Phys Rev Appl 2022;18(1):014046.
[14] Li L, Diao Y, Wu H, Jiang W. Thickness-designable acoustic metamaterial for passive phased arrays. Appl Acoust 2022;198:108942.
[15] Hur S, Jeon H, Anzan-Uz-Zaman Md, Kim Y, Shah MA, Kim J, et al. Subwavelength ultrasonic imaging via a harmonic resonant tunneling metalens. Int J Mech Sci 2022;224:107339.

[16] Chen J, Sun Z, Rao J, Lisevych D, Fan Z. Escalated Deep-Subwavelength Acoustic Imaging with Field Enhancement Inside a Metalens. Phys Rev Appl 2021;16 (4):044021.
[17] Han Y, Chen J, Fan Z. Broadband characterization of near-field focusing with groove-structured lens. IEEE Access 2021;9:46061–7.
[18] Chiang YK, Quan Li, Peng Y, Sepehrirahnama S, Oberst S, Alù A, et al. Scalable metagrating for efficient ultrasonic focusing. Phys Rev Appl 2021;16 (6):064014.
[19] Lu C, Yu R, Ma Q. GRIN metamaterial generalized Luneburg lens for ultra-long acoustic jet. Appl Phys Lett 2021; 118(14): 144103.
[20] Ma F, Zhang H, Du P, Wang C, Wu JH. An underwater planar lens for broadband acoustic concentrator. Appl Phys Lett 2022;120(12):121701.
[21] Kim C, Kim J, Jeon W. Realization of an acoustic metalens exhibiting broadband high transmission. J Sound Vib 2022;529:116910.
[22] Li H H, Zheng B, Duan M S. Helmholtz-Structured Two-Dimensional Super-Diffraction Meta-Lens. Front Phys-lausanne 2022; 529.
[23] Jin Y, Wang W, Khelif A, Djafari-Rouhani B. Elastic metasurfaces for deep and robust subwavelength focusing and imaging. Phys Rev Appl 2021;15 (2):024005.
[24] Li X, Li J, Huang XJ. Acoustic Meta-Lens for Enhanced Sensing Consisting of Single-Helicoid Array. IEEE Sens J 2022;22(14):13989–98.
[25] Cao WK, Zhang C, Wu LT, Guo KQ, Ke JC, Cui TJ, et al. Tunable acoustic metasurface for three-dimensional wave manipulations. Phys Rev Appl 2021;15(2):024026.
[26] Cao W K, Wu L T, Zhang C, et al. A reflective acoustic meta-diffuser based on the coding meta-surface. J Appl Phys 2019; 126: 194503.
[27] Zhang C, Cao W K, Wu L T, et al. A reconfigurable active acoustic metalens. Appl Phys Lett 2021; 118: 133502.
[28] Tang S, Ren B, Feng Y. Broadband acoustic focusing via binary rectangular cavity/Helmholtz resonator metasurface. J Appl Phys 2021; 129(15): 155307.
[29] Zhao S-D, Dong H-W, Miao X-B, Wang Y-S, Zhang C. Broadband coding metasurfaces with 2-bit manipulations. Phys Rev Appl 2022;17(3):034019.
[30] Chen D-C, Zhu X-F, Wei Qi, Yao J, Wu D-J. Broadband tunable focusing lenses by acoustic coding metasurfaces. J Phys D Appl Phys 2020;53(25):255501.
[31] Fokin V, Ambati M, Sun C, Zhang X. Method for retrieving effective properties of locally resonant acoustic metamaterials. Phys Rev B 2007;76(14):144302.
[32] Zheng Bo, Liu Z, Liu B, Chen X, An D, Cao G, et al. High-Throughput Superresolved Focal Imaging Based on a Phase-Modulated Acoustic Superoscillatory Lens. Phys Rev Appl 2022;18(1):014048.
[33] Zhu X, Li K, Zhang P, Zhu J, Zhang J, Tian C, et al. Implementation of dispersion-free slow acoustic wave propagation and phase engineering with helical-structured metamaterials. Nat Commun 2016;7(1).
[34] YDing Y, Statharas E C, Yao K. A broadband acoustic metamaterial with impedance matching layer of gradient index. Appl Phys Lett 2017; 110(24): 241903.
[35] Liang S, Liu T, Chen F, Zhu J. Theoretical and experimental study of gradient-helicoid metamaterial. J Sound Vib 2019;442:482–96.
[36] Xie B, Tang K, Cheng H, Liu Z, Chen S, Tian J. Coding acoustic metasurfaces. Adv Mater 2017;29(6):1603507.
[37] Fan X D, Zhu Y F, Liang B. Broadband convergence of acoustic energy with binary reflected phases on planar surface. Appl Phys Lett 2016; 109(24): 243501.
[38] Yu G, Zou X, Wang P. Achromatic acoustic generalized phase-reversal zone plates. New J Phys 2022;24(8):083009.
[39] Chen J, Xie J, Liu J. Continuous-phase-transformation acoustic metasurface. Results Phys 2021;30:104840.
[40] Rocca P, Haupt RL, Massa A. Sidelobe reduction through element phase control in uniform subarrayed array antennas. IEEE Antenn Wirel PR 2009;8:437–40.
[41] Ilovitsh A, Ilovitsh T, Ferrara KW. Multiplexed ultrasound beam summation for side lobe reduction. Sci Rep-UK 2019;9:13961.